An Improved Urban Area Extraction Method for PolSAR Data Using Eigenvalues and Optimal Roll-Invariant Features

Yu Wang, Weidong Yu, *Member, IEEE*, Ruishi Wang, Li Wang, Daqing Ge, Xiuqing Liu, Chunle Wang, and Bin Liu

***Abstract*—Urban area extraction using polarimetric synthetic aperture radar (PolSAR) data is an important application for urban planning and disaster assessment. Due to the variability in urban structures, the problem of mistaking built-up areas for vegetation remains challenging. Then, a new urban extraction method is proposed using eigenvalues and optimal roll-invariant features. First, similar to the entropy/anisotropy plane, a 2-D RVI/PA plane is adopted to construct the extractor of surface scattering areas. Then, the optimal ratio of the correlation coefficient is proposed as an extractor to depict the scattering characteristics of buildings with various orientation angles, while restraining the scattering characteristics of other land covers. In addition, reliable hidden features are selected to refine the extraction results. Finally, the spatial information extraction and classification methods are introduced to automatically determine the thresholds of the parameters above, based on which the urban area extraction map can be obtained. *C*-band Gaofen-3 SAR data collected in Runan, Henan Province, China, and San Francisco, USA, and *L*-band E-SAR data collected in Oberpfaffenhofen, Germany, are used to validate the performance of the proposed method. Experimental results demonstrate that the method can distinguish between urban and natural areas with high accuracy and has good visual effects in extracting building areas.**

***Index Terms*—Eigenvalue-based method, hidden features selection, optimal ratio of correlation coefficient, polarimetric synthetic aperture radar (PolSAR), urban area extraction.**

I. Introduction

With the advancement of satellites featuring polarimetric synthetic aperture radar (PolSAR) capabilities and ongoing research in PolSAR technology, the applicability and relevance of PolSAR data in various fields have garnered significant attention [1], [2]. The extraction of urban areas, a key application of PolSAR, plays a crucial role in evaluating disaster damage and has wide-ranging implications for both military and civilian applications [3], [4], [5], [6], [7]. Currently, urban area extraction remains a focal point of research within the PolSAR community. Accurate urban area extraction methods enable clear delineation of urban expansion and contraction, facilitating efficient reconstruction planning and economic savings. Extensive research has confirmed the promise of utilizing PolSAR data for urban area representation [8], [9], [10], [11], [12], [13]. Employing comprehensive PolSAR data across four channels enables the use of polarimetric coherences for characterizing man-made targets and classifying land cover.

Up to now, methods for building extraction have been primarily categorized into three types. 1) Polarimetric SAR target decomposition techniques, which ascertain the scattering mechanisms of various terrain types. Here, buildings are identified primarily through double-bounce scattering, with refinements achieved by enhancing decomposition models or integrating additional scattering components. 2) Statistical analysis-based methods, involving the creation of feature parameters or effective unsupervised planes, facilitate building extraction by applying appropriate thresholds. 3) Machine and deep learning approaches, which utilize tailored training samples and models to achieve accurate building extraction. This section will detail each of these methodologies.

In recent decades, polarimetric decomposition methods have predominantly been researched based on physical scattering mechanisms, which are instrumental in accurately interpreting various land covers. Kajimoto et al. [14] developed an urban area extraction method utilizing polarization orientation angle (POA) randomness between neighboring pixels to differentiate urban areas from others. Subsequently, Azmedroub et al. [15] introduced an enhanced method using Yamaguchi's four-component decomposition, circular polarization basis coefficients, and a maximum likelihood (ML) classifier [16]. Susaki et al. [17] proposed an *X*-band image-based urban extraction technique by mitigating POA effects, employing a classifier that leverages *X*-band scattering characteristics in land cover. Xiang et al.[4], [18] advanced a novel PolSAR data urban extraction

Manuscript received 16 October 2023; revised 29 November 2023, 4 January 2024, and 28 January 2024; accepted 25 February 2024. Date of publication 5 March 2024; date of current version 18 March 2024. This work was supported by the National Key Research and Development Program of China under Grant 2021YFC3000400. *(Corresponding author: Daqing Ge.)*

Yu Wang, Daqing Ge, and Bin Liu are with the China Aero Geophysical Survey and Remote Sensing Center for Natural Resources, Key Laboratory of Airborne Geophysics and Remote Sensing Geology, Ministry of Natural Resources, Beijing 100083, China (e-mail: wangyu370705@163.com; gedaqing@mail.cgs.gov.cn.).

Weidong Yu, Xiuqing Liu, and Chunle Wang are with the Department of Space Microwave Remote Sensing System, Aerospace Information Research Institute, Chinese Academy of Sciences, Beijing 100190, China, and also with the University of Chinese Academy of Sciences, Beijing 100039, China.

Ruishi Wang is with the Weifang Special Equipment Inspection and Research Institute, Shandong 261071, China.

Li Wang is with the S&A, CSIRO, Bentley, WA 6102, Australia.

Digital Object Identifier 10.1109/JSTARS.2024.3372504

approach through a multicomponent decomposition method and a unique average polarimetric coherence coefficient ratio. Hu et al. [19] improved decomposition methodology using a pure volume scattering model, effectively interpreting overestimation of volume scattering (OVS). The building scattering mechanism predominantly involves double-bounce scattering from dihedral structures formed by vertical walls and the ground. This double-bounce model is crucial for urban area extraction [20]. Specifically, when the azimuth rotation angle to the vertical wall direction is small, the symmetrical dihedral structure creates intense co-pol power, enabling double-bounce scattering to identify buildings. However, model-based decompositions also produce cross-pol power from vegetation and buildings with large orientation angles (LOBs) [21]. Thus, when the rotation angle significantly deviates, misjudgments in scattering mechanisms occur, often leading to buildings being misclassified as vegetation. Furthermore, the "Burbank" study from the Seasat SAR program indicated that flooded forests or those with wet floors generate strong double-bounce scattering, resulting in OVS and potential misclassification of buildings [22], [23]. Consequently, relying solely on decomposition results for building extraction can result in errors.

To mitigate the reliance of building extraction results on decomposition outcomes, various feature parameters have been employed or developed to enhance the building area extraction methodology. Lee et al. [1] introduced three parameters—entropy (H), the averaged angle ($\bar{\alpha}$), and anisotropy (A). The $H/\bar{\alpha}/A$ plane is effectively used to represent building areas. In their approach, Quan et al. [10] combined the radar vegetation index (RVI) with the polarimetric asymmetry (PA), proposing the RVI/PA plane to construct extractors for water bodies and buildings with various orientation angles. In addition, data-driven thresholds for these extractors were explored and established. Wang et al. [24] merged total power (Span) with the polarimetric interferometric similarity parameter (PISP), devising a Span/PISP plane for building area extraction. Hu et al. [19] developed a novel urban revised rate to interpret building areas, significantly reducing misextraction. While feature parameters in building extraction can overcome the limitations of incomplete decomposition results, existing methods often rely on data-driven thresholds determined by histogram statistics or manual judgment, potentially compromising the universality of these thresholds in building extraction applications.

In recent years, the burgeoning field of machine learning and deep learning has significantly influenced the development of building extraction methods, offering improved algorithms noted for their efficiency and reliability. Ai et al. [25] introduced a novel convolutional neural network (CNN) model, the multikernel-size feature fusion CNN (MKSFF-CNN), for SAR target classification, effectively categorizing urban areas. Li et al. [26] developed the multisource CD UNet++ (MSCDUNet), a deep learning framework that integrates multispectral, SAR, and VHR data for built-up area change detection, enabling precise extraction of building areas for change detection applications. In addition, Ai et al. [27] presented an improved convolutional autoencoder (ICAE) based on texture feature fusion (TFF-ICAE) for PolSAR terrain classification, which notably enhances building area feature separation and representation. Chen et al. [5] proposed an enhanced YOLOv7 model, achieving significant accuracy improvements [5]. Furthermore, Min et al. introduced a semantic segmentation framework using HRNet for building area extraction, detecting built-up area changes over time by aggregating extraction results [28]. However, the SAR data often features a smaller number of pixel points and samples compared to those used in common machine learning and deep learning models. To address this disparity between sample size and computational load, this article proposes a novel polarimetric SAR building area extraction method, combining machine learning concepts with traditional polarimetric SAR information extraction techniques.

In this article, we propose a novel, roll-invariant method for accurately extracting building areas, unaffected by orientation angles. The principal contributions of this study are as follows.

1) Utilization of the RVI/PA plane and the extractor P_{WB} to eliminate the impact of terrain types, predominantly characterized by surface scattering, on building extraction accuracy. Adaptive thresholding for P_{WB} is introduced to reduce human factor influence.
2) Introduction of the optimal ratio of the correlation coefficient for extracting buildings with various orientation angles, complemented by the selection of optimal hidden features to enhance extraction outcomes.
3) Implementation of a spatial information extraction method and a classification approach to autonomously determine appropriate thresholds for the aforementioned parameters.

The rest of this article is organized as follows. Section II introduces the parameters RVI, PA, the optimal ratio of the correlation coefficient, and hidden features, along with the methodology for auto-determining the thresholds of these parameters. Section III describes experimental studies using *C*-band GF-3 SAR data and *L*-band E-SAR data, validating the effectiveness of the proposed method through comparisons with existing techniques. Finally, Section IV concludes this article.

II. Methodology

A. Eigenvalue-Based Parameters

The eigenvalues and eigenvectors calculated from the 3×3 Hermitian polarimetric coherency matrix T_3 can transform the coherency matrix into a diagonalization form. T_3 can be decomposed into the sum of three unrelated targets, and each independent scattering target can be represented by a scattering matrix. The decomposition process of the coherency matrix is described as follows:

$$T_3 = \sum_{i=1}^{3} \lambda_i T_{3i} = \sum_{i=1}^{3} \lambda_i u_i u_i^{\mathrm{H}} \tag{1}$$

where the real numbers $\lambda_i (i = 1, 2, 3)$ are the eigenvalues of T_3 that are used to describe the statistical weights of three normalized target components. $U_3 = [u_1 \quad u_2 \quad u_3]$ is a 3×3 unitary matrix and $u_i (i = 1, 2, 3)$ are the unit orthogonal eigenvectors.

Based on the eigenvalue decomposition, the RVI is proposed by Van Zyl [29] to analyze the scattering of vegetation areas.

The RVI is defined as follows:

$$\mathrm{RVI} = \frac{4\lambda_3}{\lambda_1+\lambda_2+\lambda_3}, 0 \le \mathrm{RVI} \le \frac{4}{3}. \tag{2}$$

If $\lambda_1 \neq 0$ and $\lambda_2 \approx \lambda_3 \approx 0$, the vegetation parameter RVI $= 0$ corresponds to thick cylinders. The dominant scattering mechanism is equivalent to the scattering mechanism of a designated point target. If $\lambda_2 \approx \lambda_3 \approx \lambda_1$, the vegetation parameter RVI $= 4/3$ corresponds to thin cylinders, and the scattering is a random noise process [30]. It can be observed that the RVI and the entropy H exhibit the same performance except for the different range of values [10].

The influence of total power must be removed by normalizing the eigenvalues so that the analyses only focus on the purely polarimetric degrees of freedom. Similar to anisotropy A introduced in [31], polarimetric asymmetry parameters PA can be used for polarimetric analyses of two different scattering mechanisms. The normalized parameter PA is defined as follows [1]:

$$\mathrm{PA} = \frac{\Lambda_1 - \Lambda_2}{\mathrm{PF}}, \mathrm{PF} = 1 - 3\Lambda_3, 0 \le \mathrm{PF}, \mathrm{PA} \le 1 \tag{3}$$

where $\Lambda_i (i = 1, 2, 3)$ are the normalized eigenvalues. Polarimetric asymmetry is similar to anisotropy in formal characterization. The relative magnitude of the two polarimetric scattering mechanisms is represented by the ratio of the sum and difference of the two eigenvalues of the polarized return.

In this article, RVI and PA are considered to improve the ability to distinguish the scattering mechanisms of different scatterers. Similar to the H/A plane, an unsupervised 2-D classification plane RVI/PA is introduced in this article. Considering the generality and simplicity of the scattering mechanism, the classification plane RVI/PA is divided into nine equal-sized parts to express different scattering mechanisms. The division boundaries are set as follows:

$$\begin{aligned} &\mathrm{PA\_low} = 0.33, \mathrm{PA\_high} = 0.67 \\ &\mathrm{RVI\_low} = 0.45, \mathrm{RVI\_high} = 0.90. \end{aligned} \tag{4}$$

It is important to note that the chosen segmentation boundaries are somewhat arbitrary and not specific to any particular dataset. As in literature [32], the lower and upper bounding lines of the RVI/PA plane can be found in a similar way

Lower bounding line:

$$\langle [T] \rangle_I = \begin{bmatrix} 1 & 0 & 0 \\ 0 & m & 0 \\ 0 & 0 & m \end{bmatrix}, m \in [0, 1] \tag{5}$$

Upper bounding line:

$$\begin{cases} \langle [T] \rangle_{II} = \begin{bmatrix} 0 & 0 & 0 \\ 0 & 1 & 0 \\ 0 & 0 & 2m \end{bmatrix}, m \in [0, 0.5] \\ \langle [T] \rangle_{II} = \begin{bmatrix} 2m-1 & 0 & 0 \\ 0 & 1 & 0 \\ 0 & 0 & 1 \end{bmatrix}, m \in [0.5, 1] \end{cases} \tag{6}$$

where m is the depolarized parameter. With the calculation completed, the classification plane RVI/PA is physically achievable in the range of RVI and PA. An extractor P_{WB} that can be used to distinguish water areas from other terrain types can be written as

$$P_{\mathrm{WB}} = \left(\frac{4}{3} - \mathrm{RVI}\right) \cdot \mathrm{PA}, 0 \le P_{\mathrm{WB}} \le \frac{4}{3}. \tag{7}$$

A deterministic target with $\lambda_2 \approx \lambda_3 \approx 0, \lambda_1 \neq 0$ follows RVI $= 0$, and the P_{WB} map corresponds to the presence of a single dominant scattering process of the waterbody (low RVI and high PA). For a completely random target, where $\lambda_1 \approx \lambda_2 \approx \lambda_3$, this yields RVI $= 4/3$ and $P_{\mathrm{WB}} = 0$. For building areas (in the case of orthogonal buildings, for example), the value of RVI is low and the value of PA is low to medium, the value of P_{WB} is much smaller than that in the waterbody. When the appropriate threshold of P_{WB} is selected, the waterbody can be well distinguished from other areas. As previously explained, the P_{WB} map exhibits the surface scattering process and suppresses other existing scattering processes.

B. Optimal Ratio of Correlation Coefficient

Polarimetric coherence, which is defined as the complex correlation coefficient, is used to characterize the target scattering mechanism. The coherence coefficient under arbitrary polarization channels S_{aa} and S_{bb} can be written as [33]

$$\gamma_{aabb} = \frac{\langle S_{aa} S_{bb}^* \rangle}{\sqrt{\left\langle |S_{aa}|^2 \right\rangle \left\langle |S_{bb}|^2 \right\rangle}} \tag{8}$$

where the coherence magnitude $|\gamma_{aabb}|$ denotes the degree of the coherence, and $\arg(\gamma_{aabb})$ denotes the phase difference between two polarization channels.

Polarimetric coherence magnitude obtained by rotation transformation can be written as

$$|\gamma_{aabb}(\theta)| = \frac{\langle |S_{aa}(\theta) S_{bb}^*(\theta)| \rangle}{\sqrt{\left\langle |S_{aa}(\theta)|^2 \right\rangle \left\langle |S_{bb}(\theta)|^2 \right\rangle}}. \tag{9}$$

Then, the maximum magnitude in the rotation domain, namely, $|\gamma(\theta)|_{\max}$, is derived by traversing the rotation angle θ within permissible values

$$|\gamma(\theta)|_{\max} = \max_{\theta \in [0, 2\pi]} |\gamma(\theta)|. \tag{10}$$

It has been demonstrated that the ratio of the correlation coefficient has better performance in discriminating urban and nonurban areas [18], but results obtained in oriented building areas are not satisfactory. To further improve the discrimination ability, an optimal coherence ratio is proposed, which maximizes the ratio between $|\gamma_{(HH-VV)-HV}(\theta)|$ and $|\gamma_{HHVV}(\theta)|$ within the rotation domain. The optimal coherence ratio can be written as

$$\gamma_{\mathrm{ratio}} = \max_{\theta \in [0, 2\pi]} \left| \frac{\gamma_{(HH-VV)-HV}(\theta)}{\gamma_{HHVV}(\theta)} \right|. \tag{11}$$

It can be seen that the value trends of $|\gamma_{(HH-VV)-HV}(\theta)|$ and $|\gamma_{HHVV}(\theta)|$ are opposite in urban areas. Therefore, the probability of discriminating urban and nonurban areas can be improved by traversing the range of angle value.

C. Polarimetric Hidden Features Derived From Uniform Polarimetric Matrix Rotation Theory

To better depict the target orientation diversity and embed the hidden information, the acquired polarimetric information can be rotated along the line of sight. Subsequently, a uniform sinusoidal function of each term of a rotated coherency matrix can be represented with mathematic transformations [34]

$$f(\theta) = A\sin\left[\omega(\theta+\theta_0)\right] + B \tag{12}$$

where A, B, ω, and θ_0 are oscillation amplitude, oscillation center, the angular frequency, and the initial angle, respectively. The new oscillation parameter set $\{A, B, \omega, \theta_0\}$ is capable of characterizing the properties of all the elements of the coherency matrix.

In order to fully depict the hidden scattering information of the rotated targets, eleven independent hidden features as $A\_\mathrm{Re}[T'_{12}]$, $A\_\mathrm{Im}[T'_{12}]$, $A\_|T'_{12}|^2$, $A\_T'_{22}$, $B\_T'_{22}$, $B\_|T'_{23}|^2$, $\theta_0\_\mathrm{Re}[T'_{12}]$, $\theta_0\_\mathrm{Im}[T'_{12}]$, $\theta_0\_\mathrm{Re}[T'_{23}]$, $\theta_0\_|T'_{12}|^2$, $\theta_0\_|T'_{23}|^2$ are acquired and the specific expressions are derived from [34]. Where $B\_T'_{ij}$ denotes the oscillation center of T'_{ij}, the other terms are defined similarly.

If all these hidden features are applied to the extraction, redundant information appears because of the correlation of the hidden features. To reduce the calculation load, a principal component analysis (PCA) algorithm [35], which is effective in reducing dimensionality and calculation load, is used to select the reliable hidden features. Three optimal hidden features, which have high reliability in classification, are selected for subsequent processing.

D. Building-Area Extraction

In order to better delineate buildings and nonbuilding areas and improve the robustness of the threshold delineation algorithm, similar to [36], a method that can be used to adaptively select the thresholds of extractors is proposed in this article. The method can effectively avoid poor robustness due to artificial selection of thresholds, and this method can be applied to various study sites. The method consists of two main steps, and detailed introductions to these two steps are described below.

1) Spatial information extraction
   Training samples and validation sets of oceans, forests, orthogonal buildings, and oriented buildings are selected first. Instead of training the original polarimetric data directly, the weighted polarimetric data that can represent the spatial information is first calculated and the training process is based on this weighted polarimetric data. The spatial information of pixel i can be written as

$$J_i = \frac{\sum_{j\in N_i^W} \eta_\beta(J_i, J_j)\cdot J_j}{\sum_{j\in N_i^W} \eta_\beta(J_i, J_j)} \tag{13}$$

   where N_i^W is a $W\times W$ rectangular window with a center of pixel i, J_i and J_j are the coherency matrix of pixel i and pixel j, respectively. η_β represents the similarity parameter obtained through the Laplace kernel function mapping, which can be written as

$$\eta_\beta(J_i, J_j) = \exp\left\{-\beta\cdot d(J_i, J_j)\right\} \tag{14}$$

   where β is a positive hyperparameter. The negative logarithm of the likelihood function p can be used to derive the distance metric and $d(J_i, J_j) = -\frac{1}{L}\ln(p)$. Then, (12) can be further transformed into $\eta_\beta(J_i, J_j) = p^{\beta/L}$. When the hyperparameter $\beta = L$, the similarity parameter is equivalent to the likelihood function.
   In (13), as the spatial information is obtained based on pixelwise basis, the image processing results are easily affected by strong noise. To overcome aforementioned disadvantage, the similarity between patch P_k^i and P_k^j, centered on pixel i and j, respectively, is used to measure the similarity between the two pixels. The distance metric in the similarity parameter can be rewritten as

$$d_{\text{patch}}(J_i, J_j) = \sum_k d\left(P_k^i, P_k^j\right) \tag{15}$$

   where P_k^i represents the kth element in the image patch with the center of pixel i. It can be seen from (15) that the hyperparameter β in the similarity parameter must be suitable considered. In the previously proposed methods, the inverse cumulative distribution function is utilized to adaptively estimate β, which was proposed by Deledalle et al. [37]. Then, β is usually estimated based on the multilook number and it is independent of the characteristics of the input data [38]. In this article, an adaptive determination scheme for β using Monte Carlo sampling is proposed as: first, a pixel is randomly selected from the entire SAR image; then, randomly extract a pixel from its neighborhood, and above selected pixel pair are used to calculate the patchwise distance. After repeated sampling operations, the statistical distribution of the entire image can be obtained. The median statistical distribution of the random distance metrics is recorded as T_h, and set $\beta = 1/T_h$.
   Furthermore, to remove the irrelevant pixels in training sets, threshold filtering is employed to select the pixels with higher similarity, and pixels with $d_{\text{patch}}(J_i, J_j) \le T_h$ are used to calculate the neighborhood space information of the center pixel. This procedure can be named as similarity coefficient truncation, and pixels selected using this method are used for subsequent processing.
2) Thresholds selection and urban-area extraction
   To obtain the urban-area extraction results, after considering spatial information, K elements are randomly selected as the class center $Y_k^{(0)}$. The superscript (0) indicates the parameter value at the zeroth iteration. The weight of the initial subdistributions are assumed equal and $\pi_k^{(0)} = 1/K$.
   For each sample J_n, the similarity parameter between J_n and kth class center is calculated as

$$\gamma_{nk}^{(i)} = \frac{\pi_k^{(i-1)}\eta_\beta\left(J_n, Y_k^{(i-1)}\right)}{\sum_{k=1}^K \pi_k^{(i-1)}\eta_\beta\left(J_n, Y_k^{(i-1)}\right)} \tag{16}$$

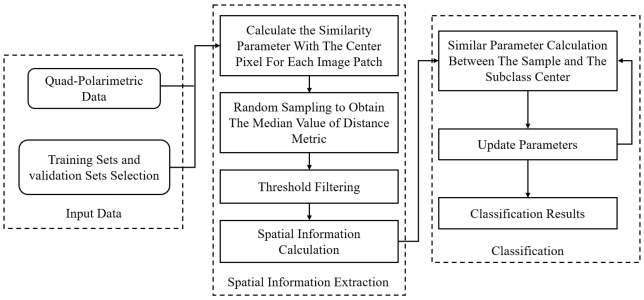

Fig. 1. Flowchart of the classification methods.

where $\gamma_{nk}^{(i)}$ is the normalized coefficient of pixel i. Then, update the class center and weight coefficient

$$Y_k^{(i)} = \frac{\sum_{n=1}^{N} \gamma_{nk}^{(i)} J_n}{\sum_{n=1}^{N} \gamma_{nk}^{(i)}} \tag{17}$$

$$\pi_k^{(i)} = \frac{1}{N} \sum_{n=1}^{N} \gamma_{nk}^{(i)}. \tag{18}$$

Repeat the above iteration process until the change value of the class center and the weight coefficient is small, terminate the iteration when

$$d\left(Y_k^{(i)}, Y_k^{(i-1)}\right) < \delta_C \tag{19}$$

$$\left|\pi_k^{(i)} - \pi_k^{(i-1)}\right| < \delta_\pi \tag{20}$$

where δ_C and δ_π represent the threshold of the class center and the weight coefficient, respectively.

After completing the above steps, the building-area extraction results obtained via P_{WB}, the optimal ratio of correlation coefficient and selected hidden features can be obtained separately. Then, fusion of correlated probabilities (FCP) technology is employed to obtain the final building extraction results. Based on the aforementioned method, the building areas (including building with various orientation angles) and nonbuilding areas (such as vegetation and water areas) can be automatically distinguished, and the urban-area extraction results can be obtained. The framework of the classification method and the flowchart of the entire framework are shown in Figs. 1 and 2, respectively.

III. Results and Discussions

A. Study Site

To validate the urban area extraction method, experimental analyses are conducted on spaceborne *C*-band GF-3 PolSAR data located in San Francisco, USA. The dimension of the image is 7681 × 5833 pixels and the resolution of the image corresponds to 8 m × 8 m. The image is subsampled with a factor of 9 in the azimuth and range directions. An optical image and the corresponding Pauli pseudocolor image of the study site are shown in Fig. 3.

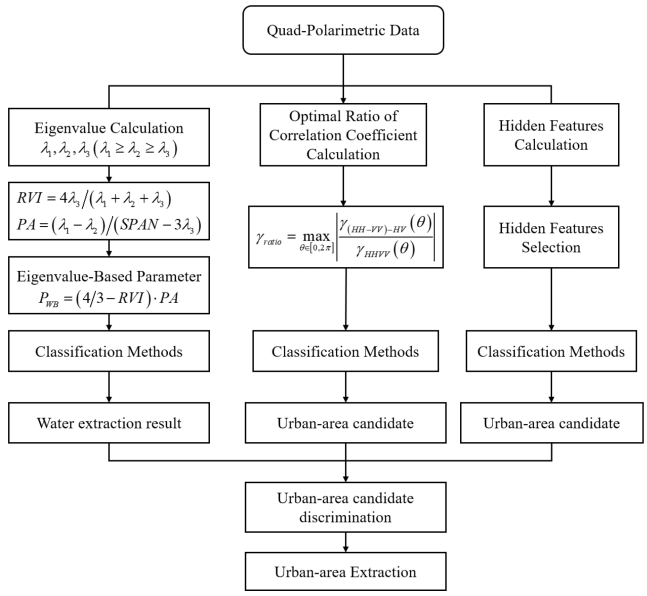

Fig. 2. Flowchart of the proposed urban-area extraction method.

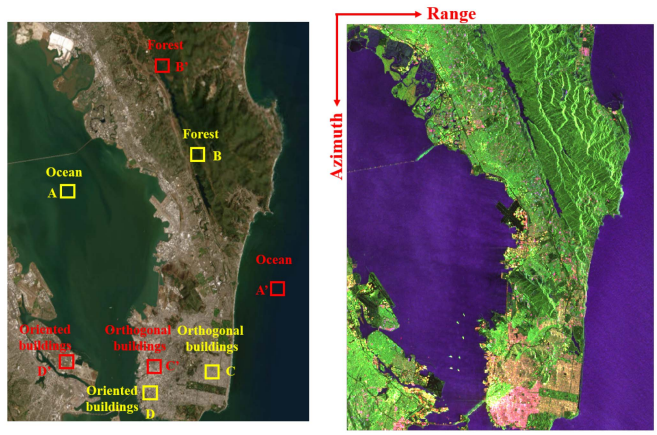

(a) (b)

Fig. 3. *C*-band GF-3 data in San Francisco, USA. (a) Optical image from Google Earth. (b) Corresponding color-coded Pauli decomposition with Red (double-bounce), Green (volume scattering), Blue (surface scattering).

B. Analysis of the Results of Building-Area Extractor

It is well known that the entropy/alpha plane is used to characterize radar backscatters. The entropy is used as a natural metric to measure the inherent reversibility of scattering data. The basic average scattering mechanism is identified by angle $\bar{\alpha}$. To distinguish the dominant scattering mechanism in polarimetric data, the plane is divided into nine zones, which correspond to different types of scattering characteristics [shown in Fig. 4(a)]. It can be observed from the preliminary classification results that although the plane can distinguish the scattering mechanism, ambiguity remains between different land covers with similar scattering mechanisms, for example, both urban and herbaceous areas are colored with pink pixels.

To expand the classification process and improve the ability to distinguish different scattering types, entropy and anisotropy can

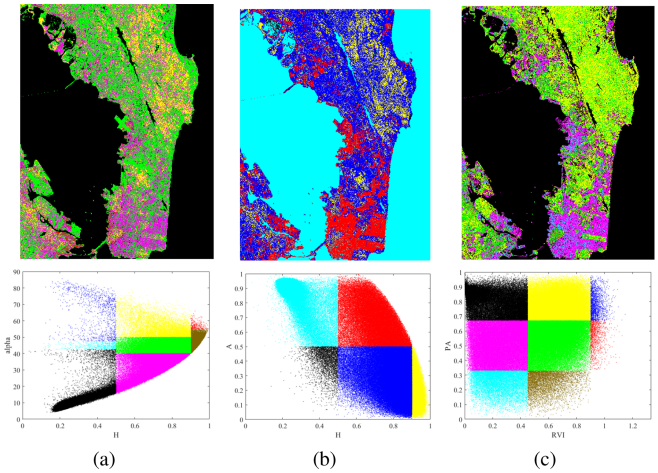

Fig. 4. Unsupervised classification using different 2-D planes. (a) Classifications and distributions using the $H/\bar{\alpha}$ plane. (b) Classifications and distributions using the H/A plane. (c) Classifications and distributions using the RVI/PA plane.

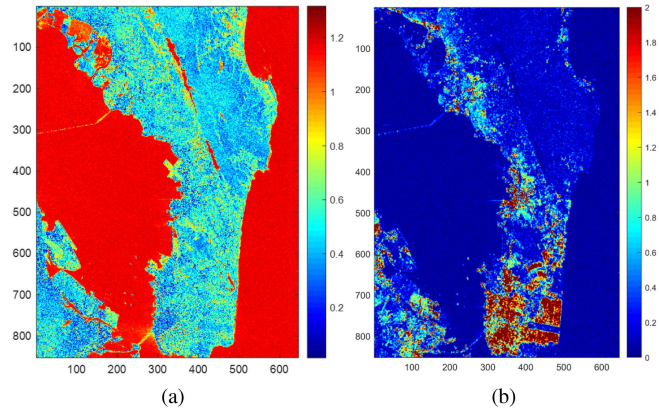

Fig. 5. Results of the extractors. (a) P_{WB}. (b) Optimal ratio of correlation coefficient.

Fig. 6. Enlarged optical images of (a) water areas, (b) forest areas, (c) orthogonal building areas, and (d) building areas with LOBs, respectively.

be combined to interpret different types of scattering behavior. The H/A plane is subdivided into six basic zones, and the preliminary classification results are shown in Fig. 4(b). The preliminary classification results reveal that the diversity of the terrain is reduced, and the scattering types in forest areas and urban areas are the same, which is not conducive to distinguishing different land covers. It has been observed in previous studies that as the number of views increases, the entropy is overestimated and the anisotropy is underestimated [31]. Therefore, the classification results of the scattering mechanism is inaccurate.

Similar to the H/A plane, an unsupervised 2-D classification plane RVI/PA is introduced in this article. Considering the generality and simplicity of the scattering mechanism, the classification plane RVI/PA is divided into nine equal-sized parts to express different scattering mechanisms. The division boundaries are set as (4). It should be noted that the segmentation boundaries not only follow the above results but also relate to the threshold of physically achievable regions. With the calculation completed, the classification plane RVI/PA is physically achievable in the range of RVI and PA. The classification results are shown in Fig. 4(c).

From Fig. 4(c), we can note that the classification results are less affected by noise. Pixels in magenta and cyan can be extracted as candidate points for the buildings with small orientation angles (SOBs). Buildings in these areas are parallel or approximately parallel to the flight direction and yield intense co-pol components. In addition, pixels in black represent surface scattering regions. Although the H/A plane can be used to describe the building areas, it is difficult to characterize the SOBs completely by segmenting the red area (medium entropy and high anisotropy). With the RVI and PA combined, the extractor P_{WB} is introduced to characterize the surface scattering, as shown in Fig. 5(a).

Fig. 5(a) shows that the P_{WB} primarily characterizes surface scattering areas, such as lakes and bare soils. The scattering power of farmland is lower than that of lakes. In this study site, P_{WB} can be used to distinguish between the water areas and other terrain types. The optimal ratio of correlation coefficient is used to distinguish between building areas and other terrain types, as shown in Fig. 5(b). In Fig. 5(b), building areas with various orientation angles can be reasonably extracted using proper thresholds.

Moreover, in Fig. 3(a), patches A–D marked in yellow rectangles are used to select the optimal hidden features. The terrain types of these selected patches are water areas, forest areas, orthogonal building areas, and building areas with LOBs, respectively. The enlarged optical images of these patched are shown in Fig. 6. According to the selection method introduced in Section II-C, three optimal hidden features, namely, $A\_\mathrm{Re}[T'_{12}]$, $A\_|T'_{12}|^2$, and $B\_T'_{22}$, are selected based on the overall classification accuracy. The histograms of selected hidden features are shown in Fig. 7. By using the classification method proposed in Section II-D, the thresholds of these features can be determined as 0.272, 0.266, and 0.303, respectively, and all these thresholds are consistent with the histogram thresholding results.

Using the aforementioned thresholds of the extractors, the extraction results of urban areas are shown in Fig. 8. Combined

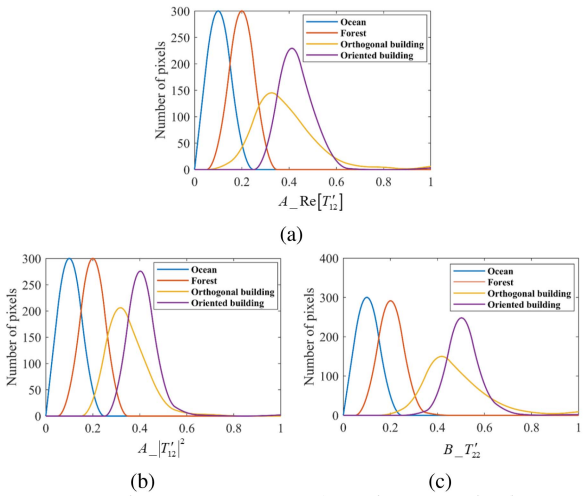

Fig. 7. Feature histograms of typical patches. (a) Histogram of $A\_\mathrm{Re}[T'_{12}]$. (b) Histogram of $A\_|T'_{12}|^2$. (c) Histogram of $B\_T'_{23}$.

TABLE I
ACCURACY OF THE EXTRACTION RESULTS OF THE STUDY SITE

Methods	UA (%)	PA' (%)	OA (%)	KP
Azmedroub	72.40	41.04	78.87	0.4286
Quan	93.51	72.16	93.79	0.7807
Hu	93.87	73.02	94.28	0.8014
Proposed	94.24	74.17	95.26	0.8122

with P_{WB}, the extraction results obtained via the optimal ratio of the correlation coefficient and hidden features are shown in Fig. 8(a) and (b), respectively. The final extraction map of the proposed method is shown in Fig. 8(c). The map shows that the misextraction pixels are well smoothed and the building areas are well described. Notice that some ships and bridges are misextracted by the proposed method (marked in red rectangles). The reason is that the scattering characteristics of these man-made targets exhibit similarities to buildings, resulting in misextraction. To further demonstrate the validity of the proposed method, the extraction results obtained via the proposed method are compared with the extraction results obtained via the methods proposed by Azmedroub et al. [16] [shown in Fig. 8(d)], Quan et al. [10] [shown in Fig. 8(e)], Hu et al. [19] [shown in Fig. 8(f)].

To quantitatively evaluate the performance of the proposed method, four indices, i.e., user's accuracy (UA), producer's accuracy (to distinguish the polarimetric asymmetry parameter PA mentioned earlier, this parameter is named PA'), overall accuracy (OA) and Kappa coefficient (KP), are used to evaluate the extraction results of the study site obtained via four methods. The accuracy evaluation results, as obtained via the aforementioned methods, are listed in Table I.

The statistical results in Table I show that the OA and KP of the proposed method are higher than those of the other three methods on the study site. In Table I and Fig. 8(d), a large number of buildings with LOBs are misclassified as nonurban areas, leading to a reduction in accuracy. In Table I and Fig. 8(e), the ridges of mountain areas are misclassified as urban areas and the number of false-alarms cannot be properly reduced, resulting in the misextraction. In Table I and Fig. 8(f), a large number of building areas with LOBs can be extracted by using the new urban revised rate, but there are still some large oriented building areas that have not been extracted. As a result, in terms of the ability to extract urban areas, the proposed method is a satisfactory extraction approach.

Based on the proceeding analyses and evaluations, it can be concluded that the proposed method is a good approach for urban area extraction.

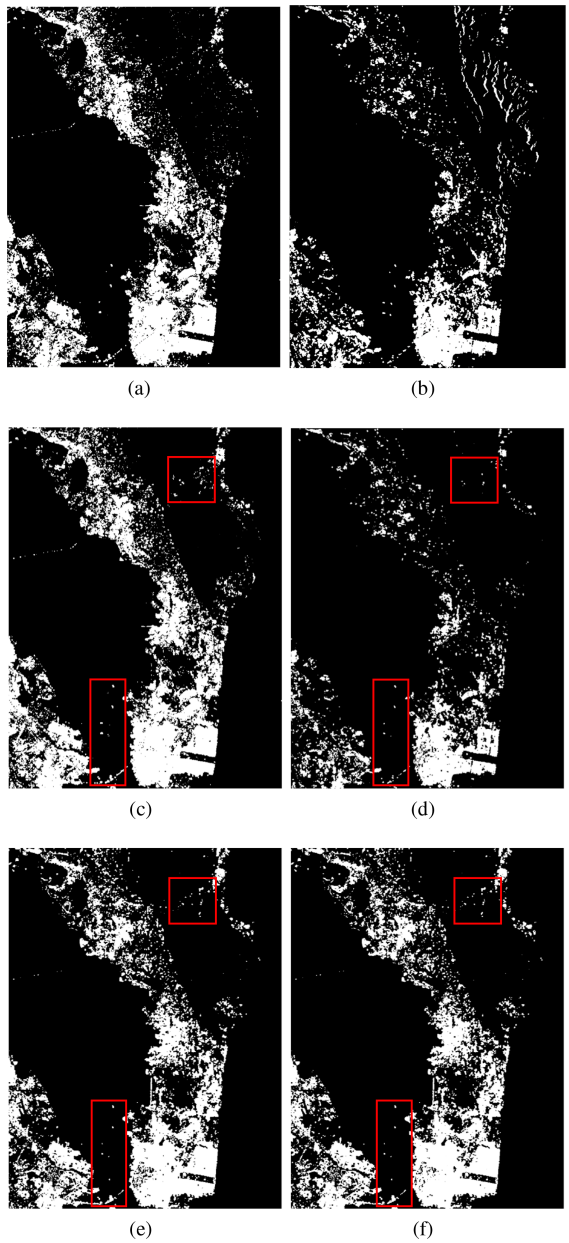

Fig. 8. Urban area extraction maps of the study site. (a) Extraction result of γ_{ratio}. (b) Extraction result of the selected hidden features. (c) Extraction result of the proposed method. (d) Extraction map obtained via the method proposed by Azmedroub et al. (e) Extraction map obtained via the method proposed by Quan et al. (f) Extraction map obtained via the method proposed by Hu et al.

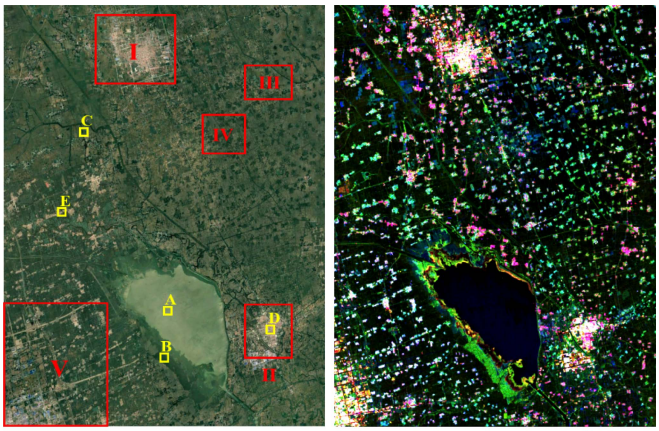

Fig. 9. Study area intercepted in Henan Province. (a) Optical image collected from Google Earth. (b) PolSAR Pauli pseudocolor map.

C. GF-3 Data Collected Over Runan, Henan Province, China

To further demonstrate the robustness of the proposed extraction method, results derived from Spaceborne *C*-band GF-3 PolSAR data, which is located in Runan, Henan Province, China, are analyzed. The study site includes buildings with different orientation angles, forests, farmlands, and lakes. Fig. 9 shows the optical image derived from Google Earth and the Pauli pseudocolor image of the study area. The size of the image is 8723×6695 pixels. The resolution of the image corresponds to 8 m×8 m, and the ensemble average of the study site is performed with factor 13 in the azimuth and range directions. A refined Lee filter has been applied to smooth the speckle effect using a 7×7 moving window.

Five typical regions (patches A–E) are manually labeled with yellow rectangles in Fig. 9(a) for the statistical analyses of thresholds of extractors. The final extraction results obtained via the proposed method are shown in Fig. 10(a). To comprehensively illustrate the extraction outcomes, the extraction results for urban areas obtained via the methods proposed by Azmedroub et al. [16], Quan et al. [10], and Hu et al. [19] are shown in Fig. 10(b), (c), and (d), respectively. Compared with the urban ground truth obtained from Google Earth [see Fig. 10(e)], the extraction result obtained by the proposed method is visually much more accurate than those obtained by other methods, e.g., the areas circled by yellow ellipses in Fig. 10. Intuitively speaking, the method proposed by Azmedroub et al. is not sufficiently accurate to extract buildings with LOBs, the method proposed by Quan et al. cannot reasonably remove the forest area in the strong scattering amplitude areas, and the method proposed by Hu et al. still needs to be further enhanced in the building areas with LOBs, resulting in the misextraction of the building areas.

The urban areas extracted at the study site are compared with the urban ground truth, as shown in Table II. As shown in Table II, the OA and KP of the extraction results obtained by the proposed algorithm are higher than those of the existing methods, and

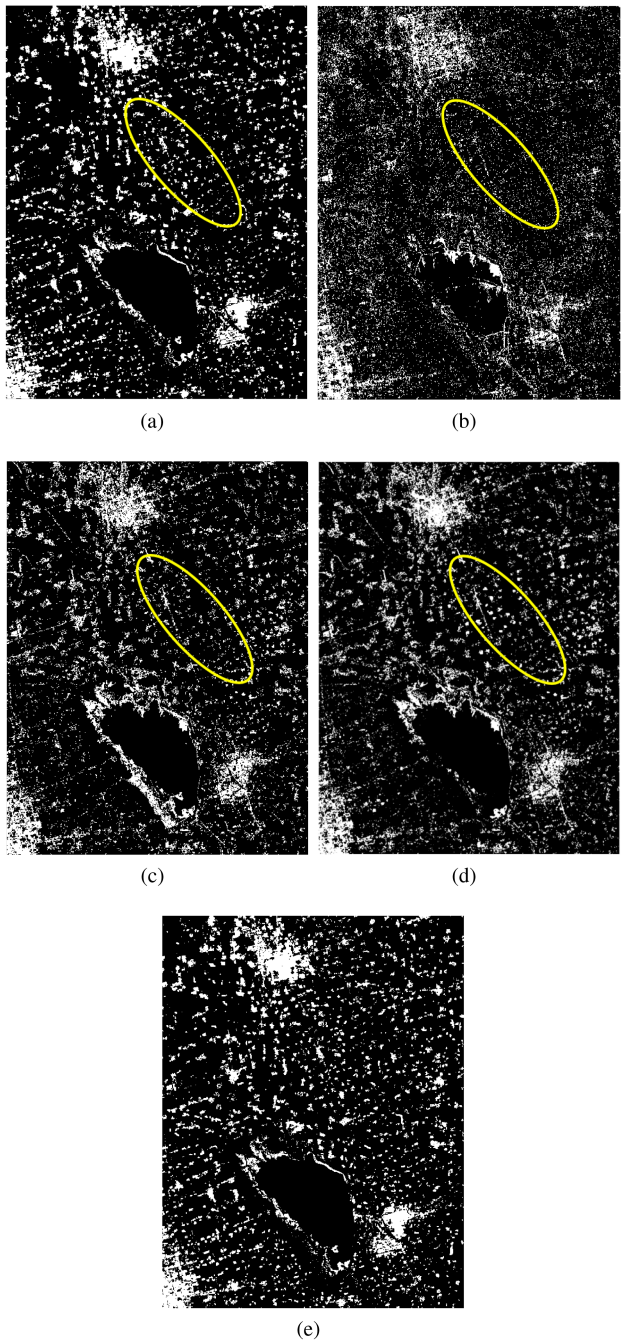

Fig. 10. Urban areas extraction results with different methods. (a)–(d) Results obtained by using the proposed method, the method in [16], the method in [10] and the method in [19], respectively. (e) Urban ground truth from Google Earth.

TABLE II
ACCURACY OF EXTRACTED URBAN AREAS FOR THE STUDY SITE

Methods	Azmedroub's method	Quan's method	Hu's method	Proposed method
OA(%)	85.31	89.43	89.77	91.35
KP	0.7857	0.8197	0.8244	0.8349

TABLE III
ACCURACY OF EXTRACTED URBAN AREAS IN ROIS

Methods	ROI I		ROI II		ROI III		ROI IV		ROI V	
	KP	OA(%)	KP	OA(%)	KP	OA(%)	KP	OA(%)	KP	OA(%)
1	0.8127	77.80	0.7877	80.80	0.5454	53.66	0.4512	46.33	0.7547	82.78
2	0.8679	82.78	0.8492	92.02	0.7642	87.41	0.6257	76.08	0.7921	86.80
3	0.8688	85.47	0.8522	92.59	0.7653	87.91	0.6124	75.57	0.8061	87.66
4	0.8746	95.49	0.8694	93.54	0.7702	89.88	0.6016	72.16	0.8544	93.02

[1] 1 – method proposed by Azmedroub et al., 2 - method proposed by Quan et al., 3 - method proposed by Hu et al., 4 – the proposed method.

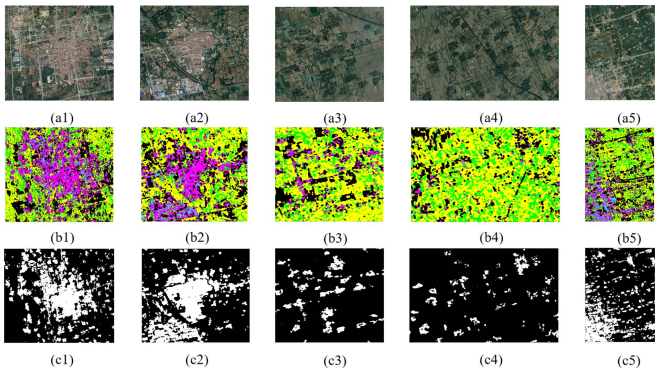

Fig. 11. Results of the selected typical patches. (a1)–(a5) Optical images. (b1)–(b5) Corresponding data distributions. (d1)–(c5) Extraction maps.

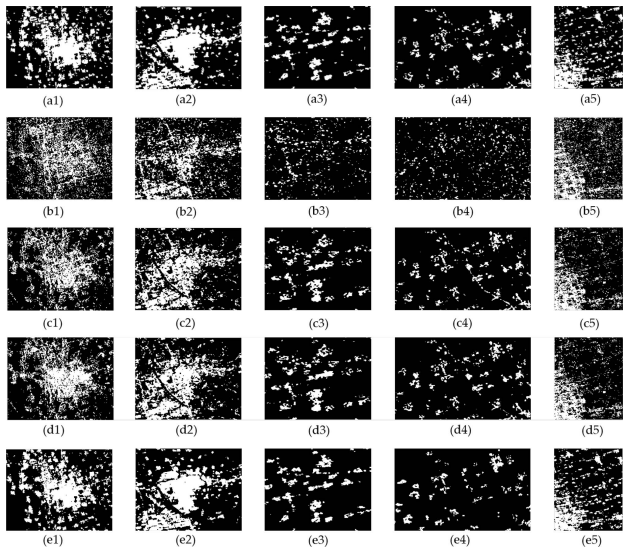

Fig. 12. Urban area extraction results for the ROIs obtained by using different methods. (a1)–(a5) Ground truth of the ROIs obtained from Google Earth. (b1)–(b5) Results obtained by Azmedroub et al. (c1)–(c5) Results obtained by Quan et al. (d1)–(d5) Results obtained by Hu et al. (e1)–(e5) Results obtained by the proposed method.

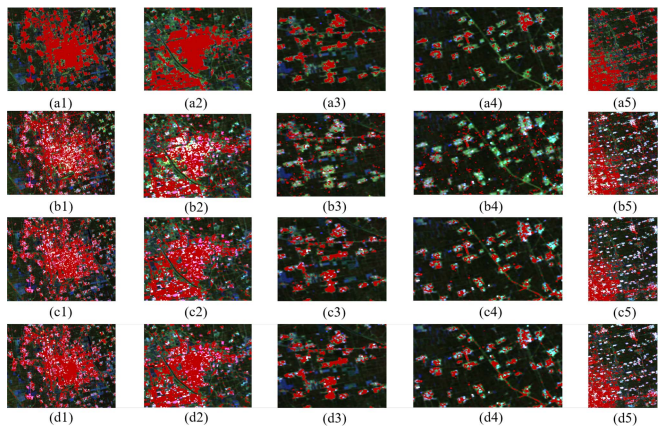

Fig. 13. Superimposed extraction results of the selected patches using the four methods on a Pauli RGB image. (a1)–(a5) Results obtained by proposed method. (b1)–(b5) Results obtained by Azmedroub et al. (c1)–(c5) Results obtained by Quan et al. (d1)–(d5) Results obtained by Hu et al.

the SAR system is reliable. For the two previously developed methods, a significant proportion of the LOBs are misidentified as nonbuilding areas, whereas the proposed method effectively resolves this issue. Therefore, the misidentification of the LOBs is the main reason why the building area cannot be accurately extracted. Because of the large range of the selected regions, five regions of interest (ROIs) are selected to analyze the accuracy of the extraction results [labeled as red rectangles I–V in Fig. 9(a)]. Analyses of typical areas facilitate the assessment of morphological protection in urban areas while providing intuitive and quantitative information on ROIs.

Furthermore, the validity and accuracy of the proposed method are evaluated through quantitative analyses of ROIs. For the ROIs, the ground truth can be obtained from Google Earth, which can be used for quantitative analysis. The results for the RVI/PA plane distribution and extractions of five typical areas are shown in Fig. 11. To better investigate the advantages of the proposed method, the ground truth, and the urban area extraction results using different methods are utilized for intuitive comparative analyses. The results are shown in Fig. 12, and the results are superimposed on the Pauli RGB image in Fig. 13 to intuitively analyze the extraction results. In Fig. 13, when a pixel point is determined to be a building point, the color of the pixel point is set to red, and when a pixel point is determined to be a nonbuilding point, the color of the pixel point is retained in the pseudocolour mapping of the result of the Pauli decomposition. Two indices, i.e., KP and OA, are used to evaluate the extraction results of the four methods for urban areas. The evaluation results obtained by the previously described methods are presented in Table III.

In ROIs, the statistical results in Table III reveal that the OA and KP of the proposed method are higher than those of the other three methods for all typical patches except patch IV. In the other three methods, a certain extent of misclassification occurs where LOBs are incorrectly identified as nonbuilding areas. In

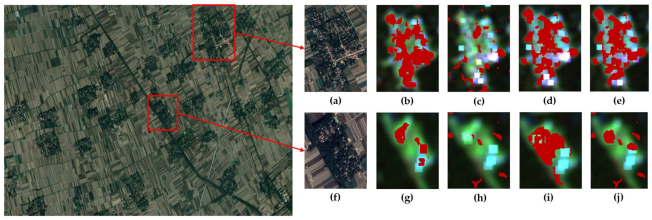

Fig. 14. Extraction results for enlarged small buildings. (a) and (f) Optical images. (b) and (g) Results obtained by the proposed method. (c) and (h) Results obtained by Azmedroub et al. (d) and (i) Results obtained by Quan et al. (e) and (j) Results obtained by Hu et al.

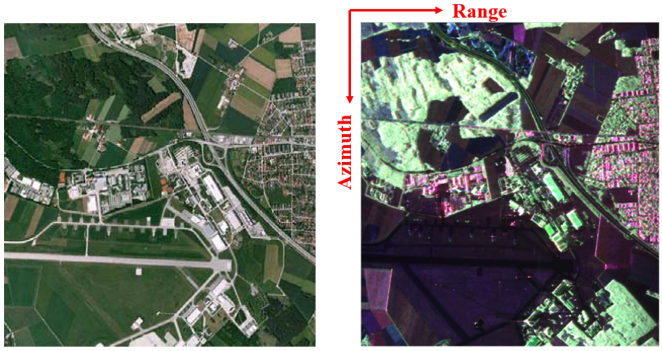

Fig. 15. SAR images of the study site over the Oberpfaffenhofen, Germany (E-SAR, *L*-band). (a) An optical image from Google Earth. (b) Color-coded Pauli decomposition with red (double-bounce), green (volume scattering), blue (surface scattering).

region IV, both the results obtained using Quan's method and the results obtained by Hu et al. are better than that of the proposed method, which is determined by the distribution characteristics of the buildings in this area. In this regard, small villages with complex structures are selected for analysis and the extraction results are provided in Fig. 14.

According to the optical images shown in Fig. 14, a number of the buildings in the selected area are scattered in the village and surrounded by vegetation. When the number of trees around a building is sufficiently large, the building submerges in the vegetation, exhibiting the characteristics of volume scattering. It can be observed in the extraction results for the enlarged small buildings that, although the proposed method may cause the loss of certain pixels of buildings, it correctly extracts the building areas while effectively depicting the contours of the building areas.

D. L-Band E-SAR PolSAR Data Over Oberpfaffenhofen, Germany

To demonstrate the robustness of the proposed method across different bands, *L*-band E-SAR repeat-pass PolSAR data from Oberpfaffenhofen, Germany, are analyzed. The study site, covering a range of terrain types, is depicted in 1300×1200 pixels. The image includes various terrain types, such as buildings with various orientation angles, farmlands, forests and airports, etc. The temporal baseline of the image is within one day and the

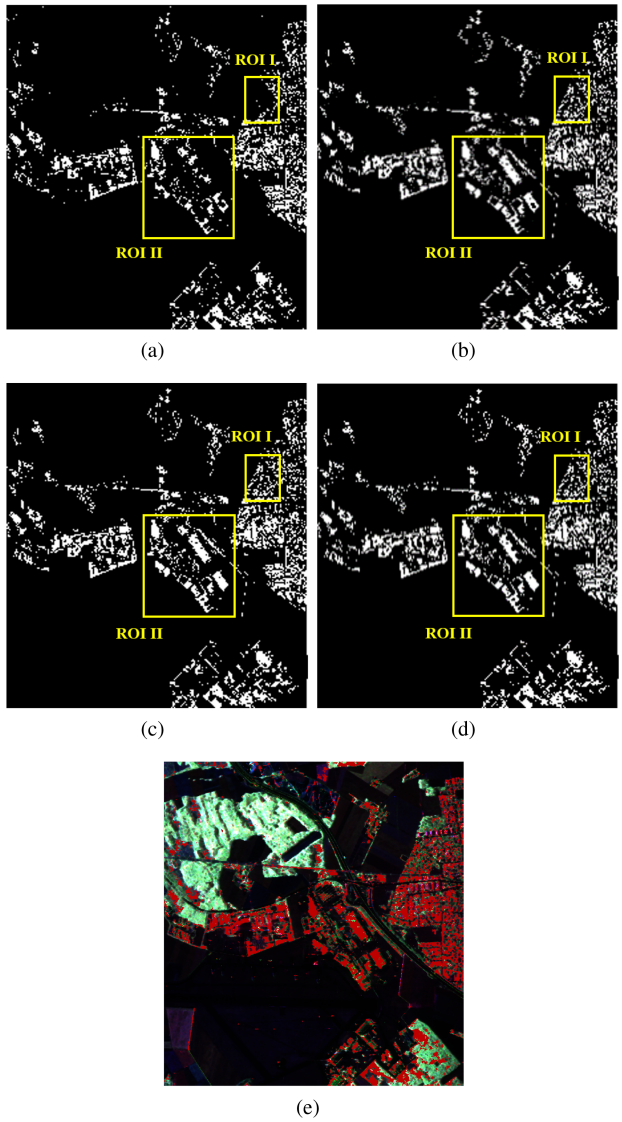

Fig. 16. Urban areas extraction results with different methods. (a)–(d) Extraction results obtained via the method in [16], the method in [10], the method in [19] and the proposed method, respectively. (e) Superimpose the extraction results obtained via the proposed method on the Pauli image.

incidence angle is about 40°. The central coordinates of the image are (48°5′3″N, 11°17′4″E). Since the equivalent number of looks in the data is high enough, no more averaging or filter is employed. The optical image of the study site and the corresponding color-coded Pauli image are shown in Fig. 15.

Urban area extraction results obtained via the method proposed by Azmedroub et al., the method proposed by Quan et al., the method proposed by Hu et al. and the method proposed in this article are shown in Fig. 16(a)–(d), respectively. The extraction results obtained via the proposed method are superimposed on the Pauli image, as shown in Fig. 16(e). For the entire urban-area extraction results obtained via different methods, compared with the existing methods, the extraction results obtained via the proposed method have better performance in the building areas, especially the building areas with LOBs.

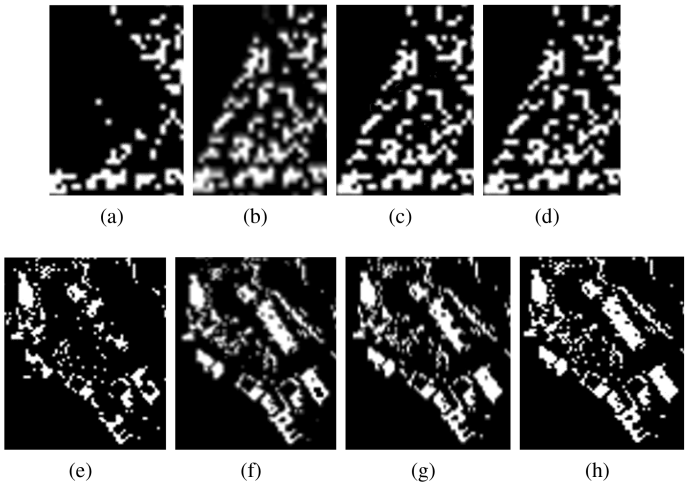

Fig. 17. Enlarged extraction results obtained via different extraction methods. (a)–(d) Results of ROI-I obtained via the method in [16], the method in [10], the method in [19] and the proposed method, respectively. (e)–(h) Results of ROI-I obtained via the method in [16], the method in [10], the method in [19] and the proposed method, respectively.

TABLE IV
ACCURACY OF EXTRACTED URBAN AREAS IN ROIS

Methods	ROI I		ROI II	
	KP	OA(%)	KP	OA(%)
1	0.6755	61.08	0.7049	72.45
2	0.8972	88.46	0.9103	93.01
3	0.9004	89.01	0.9215	93.97
4	0.9075	89.77	0.9257	94.35

[1] 1 – method proposed by Azmedroub et al., 2 - method proposed by Quan et al., 3 - method proposed by Hu et al., 4 – the proposed method.

To further evaluate the performance of the proposed method, two patches marked in yellow rectangles, namely, as ROI-I and ROI-II, are selected in Fig. 16. Enlarged extraction results obtained via different extraction methods are shown in Fig. 17. In Fig. 17, the dominant terrain type of the ROIs is buildings with LOBs. The ROI-II has an approximate orientation angle of 45°, which brings great challenges to the accuracy of building area extraction. According to Fig. 17, compared with existing extraction methods, the extraction results obtained via the proposed method can reasonably characterize the building areas, which have better correspondence with the ground truth.

Similar to the evaluation approach used earlier in this article, two indices, namely, KP and OA, are utilized to assess the urban area extraction results of the four methods. The evaluation results obtained by the previously described methods are presented in Table IV.

The statistical results in Table IV reveal that the OA and KP of the proposed method are higher than those of the other three methods for the selected building areas with LOBs. In the other three methods, a number of LOBs are incorrectly identified as nonbuilding areas, which leads to the reduction of the OA and KP of the ROIs. In ROIs, the results obtained via Quan's method are better than that of the Azmedroub's method, which is determined by the distribution characteristics of the buildings in this area. In addition, the building extraction results obtained via Hu's method are superior to those obtained by Azmedroub's method, proving that the validity of the decomposition results is decisive for the final building extraction results.

IV. CONCLUSION

The method proposed in this article utilizes eigenvalues and optimal roll-invariant parameters to extract the building areas with different orientation angles. The RVI/PA plane provides a simple unsupervised classification strategy while emphasizing the geometric segmentation of physical scattering processes, providing support for the construction of extractor that can be used to distinguish between regions dominated by surface scattering and others. Using selected training sets, thresholds for the building area extractors are determined by using spatial information extraction and classification processing, the optimal ratio of correlation coefficient and hidden features are used as the extractor to extract buildings with different orientation angles. By fusing the extraction results of extractors P_{WB} and the optimal ratio of correlation coefficient, the urban area candidates can be obtained. In addition, the presence of noise leads to misextraction in certain areas. To overcome these defects, the optimal hidden features, i.e., those that can best represent the polarimetric hidden land-cover information, are selected as a supplement to the urban area extraction result, and the impact of noise points and the dispersion of classification results can be effectively reduced. The validation and effectiveness of the proposed method are demonstrated using data collected over different study sites and different bands, and the proposed method is satisfactory with high OA and a high KP. Therefore, based on the research and analyses, we conclude that our method represents a robust approach for urban area extraction.

IV. ACKNOWLEDGMENT

The authors acknowledge the support of the Resource Satellite Application Center for providing Gaofen-3 full polarimetric data.

REFERENCES

[1] J. S. Lee and E. Pottier, "Polarimetric radar imaging: From basics to applications," *Francis Group Boca Raton ISBN*, 2009. [Online]. Available: https://www.taylorfrancis.com/books/mono/10.1201/9781420054989/polarimetric-radar-imaging-jong-sen-lee-eric-pottier

[2] Y. Hu, J. Fan, and J. Wang, "Classification of PolSAR images based on adaptive nonlocal stacked sparse autoencoder," *IEEE Geosci. Remote Sens. Lett.*, vol. 15, no. 7, pp. 1050–1054, Jul. 2018.

[3] L. Zhao, J. Yang, P. Li, L. Zhang, L. Shi, and F. Lang, "Damage assessment in urban areas using post-earthquake airborne PolSAR imagery," *Int. J. Remote Sens.*, vol. 34, pp. 8952–8966, 2013.

[4] D. Xiang, Y. Ban, and Y. Su, "Model-based decomposition with cross scattering for polarimetric SAR urban areas," *IEEE Geosci. Remote Sens. Lett.*, vol. 12, no. 12, pp. 2496–2500, Dec. 2015.

[5] L. Chen, L. Cao, F. Meng, and F. Ma, "Semantic segmentation of built-up areas in SAR images based on improved YOLOV7 model," in *Proc. SAR Big Data Era*, 2023, pp. 1–4.

[6] J. Ai, Y. Mao, Q. Luo, L. Jia, and M. Xing, "Multi-scale rotation- invariant haar-like feature integrated CNN based ship detection algorithm of multiple- target environment in SAR imagery," *IEEE Trans. Geosci. Remote Sens.*, vol. 57, no. 12, pp. 10070–10087, Dec. 2019.

[7] J.-W. Deng, M.-D. Li, H.-L. Li, and S.-W. Chen, "Urban damage mapping with reconstructed quad-pol SAR data from dual-pol SAR mode,"

in *Proc. XXXVth Gen. Assem. Sci. Symp. Int. Union Radio Sci.*, 2023, pp. 1–4.
[8] L. Deng and C. Wang, "Improved building extraction with integrated decomposition of time-frequency and entropy-alpha using polarimetric SAR data," *IEEE J. Sel. Topics Appl. Earth Observ. Remote Sens.*, vol. 7, no. 10, pp. 4058–4068, Oct. 2014.
[9] S. Quan, B. Xiong, D. Xiang, and G. Kuang, "Derivation of the orientation parameters in built-up areas: With application to model-based decomposition," *IEEE Trans. Geosci. Remote Sens.*, vol. 56, no. 8, pp. 4714–4730, Aug. 2018.
[10] S. Quan, B. Xiong, and D. Xiang, "Eigenvalue-based urban area extraction using polarimetric SAR data," *IEEE J. Sel. Topics Appl. Earth Observ. Remote Sens.*, vol. 11, no. 2, pp. 458–471, Feb. 2018.
[11] D. Ratha, P. Gamba, A. Bhattacharya, and A. C. Frery, "Novel techniques for built-up area extraction from polarimetric SAR images," *IEEE Geosci. Remote Sens. Lett.*, vol. 17, no. 1, pp. 177–181, Jan. 2020.
[12] S. Dey, N. Bhogapurapu, A. Bhattacharya, A. C. Frery, and P. Gamba, "Built-up area mapping using full and dual polarimetric SAR data," in *Proc. IEEE Int. Geosci. Remote Sens. Symp.*, 2021, pp. 1693–1696.
[13] R. Adhikari and K. Jain, "Urban built-up extraction using SAR polarimetry with feature combination and machine learning technique," in *Proc. Int. Conf. Comput. Electron. Electr. Eng. Appl.*, 2023, pp. 1–7.
[14] M. Kajimoto and J. Susaki, "Urban area extraction from polarimetric SAR images using polarization orientation angle," *IEEE Geosci. Remote Sens. Lett.*, vol. 10, no. 2, pp. 337–341, Mar. 2013.
[15] Y. Yamaguchi, A. Sato, W. M. Boerner, R. Sato, and H. Yamada, "Four-component scattering power decomposition with rotation of coherency matrix," *IEEE Trans. Geosci. Remote Sens.*, vol. 49, no. 6, pp. 2251–2258, Jun. 2011.
[16] B. Azmedroub, M. Ouarzeddine, and B. Souissi, "Extraction of urban areas from polarimetric SAR imagery," *IEEE J. Sel. Topics Appl. Earth Observ. Remote Sens.*, vol. 9, no. 6, pp. 2583–2591, Jun. 2016.
[17] J. Susaki and M. Kishimoto, "Urban area extraction using X-band fully polarimetric SAR imagery," *IEEE J. Sel. Topics Appl. Earth Observ. Remote Sens.*, vol. 9, no. 6, pp. 2592–2601, Jun. 2016.
[18] D. Xiang, T. Tang, C. Hu, Q. Fan, and Y. Su, "Built-up area extraction from PolSAR imagery with model-based decomposition and polarimetric coherence," *Remote Sens.*, vol. 8, pp. 1–21, 2016. .
[19] C. Hu, Y. Wang, X. Sun, S. Quan, and D. Xiang, "Model-based polarimetric target decomposition with power redistribution for urban areas," *IEEE J. Sel. Topics Appl. Earth Observ. Remote Sens.*, vol. 16, pp. 8795–8808, 2023.
[20] H. Li, Q. Li, G. Wu, J. Chen, and S. Liang, "The impacts of building orientation on polarimetric orientation angle estimation and model-based decomposition for multilook polarimetric SAR data in urban areas," *IEEE Trans. Geosci. Remote Sens.*, vol. 54, no. 9, pp. 5520–5532, Sep. 2016.
[21] S. Hong and S. Wdowinski, "Double-bounce component in crosspolarimetric SAR from a new scattering target decomposition," *IEEE Trans. Geosci. Remote Sens.*, vol. 52, no. 6, pp. 3039–3051, Jun. 2014.
[22] L. L. Hess, J. M. Melack, S. Filoso, and Y. Wang, "Delineation of inundated area and vegetation along the Amazon floodplain with the SIR-C synthetic aperture radar," *IEEE Trans. Geosci. Remote Sens.*, vol. 33, no. 4, pp. 896–904, Jul. 1995.
[23] Y. Wang and F. W. Davis, "Decomposition of polarimetric synthetic aperture radar backscatter from upland and flooded forests," *Int. J. Remote Sens.*, vol. 18, no. 6, pp. 1319–1332, 1997.
[24] Y. Wang, W. Yu, and W. Hou, "Five-component decomposition methods of polarimetric SAR and polarimetric SAR interferometry using coupling scattering mechanisms," *IEEE J. Sel. Topics Appl. Earth Observ. Remote Sens.*, vol. 14, pp. 6662–6676, 2021.
[25] J. Ai, Y. Mao, Q. Luo, L. Jia, and M. Xing, "SAR target classification using the multi-kernel-size feature fusion based convolutional neural network," *IEEE Trans. Geosci. Remote Sens.*, vol. 60, 2022, Art. no. 5214313.
[26] H. Li, F. Zhu, X. Zheng, M. Liu, and G. Chen, "MSCDUNet: A deep learning framework for built-up area change detection integrating multispectral, SAR, and VHR data," *IEEE J. Sel. Topics Appl. Earth Observ. Remote Sens.*, vol. 15, pp. 5163–5176, 2022.
[27] J. Ai et al., "A fine PolSAR terrain classification algorithm using the texture feature fusion based improved convolutional autoencoder," *IEEE Trans. Geosci. Remote Sens.*, vol. 60, 2022, Art. no. 5218714.
[28] N. Min, S. Tian, F. Wu, C. Wang, H. Zhang, and B. Zhang, "Built-up area extraction and analysis with multi-temporal SAR images based on HRNETV2," in *Proc. IEEE Int. Geosci. Remote Sens. Symp.*, 2023, pp. 3644–3647.
[29] J. Van Zyl, "Application of cloude's target decomposition theorem to polarimetric imaging radar," *SPIE*, vol. 127, pp. 184–212, 1992.
[30] J. J. van Zyl and Y. Kim, *Synthetic Aperture Radar Polarimetry*. Pasadena, CA, USA: Wiley, 2011.
[31] S. Cloude and E. Pottier, "A review of target decomposition theorems in radar polarimetry," *IEEE Trans. Geosci. Remote Sens.*, vol. 34, no. 2, pp. 498–518, Mar. 1996.
[32] S. Cloude, *Polarisation: Applications in Remote Sensing*. New York, NY, USA: Oxford Univ. Press, 2010.
[33] T. L. Ainsworth, D. L. Schuler, and J. S. Lee, "Polarimetric SAR characterization of man-made structures in urban areas using normalized circular-pol correlation coefficients," *Remote Sens. Environ.*, vol. 112, no. 6, pp. 2876–2885, 2008.
[34] S. Chen, X. Wang, and M. Sato, "Uniform polarimetric matrix rotation theory and its applications," *IEEE Trans. Geosci. Remote Sens.*, vol. 52, no. 8, pp. 4756–4770, Aug. 2014.
[35] J. O'Brien, "Correlated probability fusion for multiple class discrimination," in *Proc. Inf. Decis. Control*, 1999, pp. 571–577.
[36] G. J. McLachlan and T. Krishnan, *The EM Algorithm and Extension*, vol. 382. Hoboken, NJ, USA: Wiley, 2007.
[37] C. A. Deledalle, L. Denis, and F. Tupin, "Iterative weighted maximum likelihood denoising with probabilistic patch-based weights," *IEEE Trans. Image Process.*, vol. 18, no. 12, pp. 2661–2672, Dec. 2009.
[38] H. Zhong, J. Zhang, and G. Liu, "Robust polarimetric SAR despeckling based on nonlocal means and distributed Lee filter," *IEEE Trans. Geosci. Remote Sens.*, vol. 52, no. 7, pp. 4198–4210, Jul. 2014.

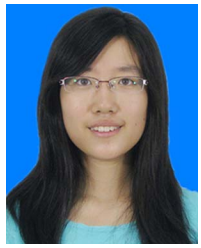

Yu Wang received the bachelor's degree in telecommunication engineering from Jilin University, Jilin, China, in 2016, and the Ph.D. degree in communication and information systems from the Graduate University of Chinese Academy of Sciences, Beijing, China, in 2021.

Currently, she is working as a Research Assistant in SAR image processing with the China Aero Geophysical Survey and Remote Sensing Center for Natural Resources, Beijing. Her current research interests include polarimetric SAR technology, interferometric SAR technology, polarimetric SAR interferometry, and geohazards monitoring applications.

Weidong Yu (Member, IEEE) was born in Henan, China, in 1969. He received the M.Sc. and Ph.D. degrees in electrical engineering from the Nanjing University of Aeronautics and Aerospace, Nanjing, China, in 1994 and 1997, respectively.

He has been with the Institute of Electronic, Chinese Academy of Science (IECAS), since 1997, and became a Professor of communication and information systems in 2000. He has authored more than 50 papers and holds five patents. He has been the Chief Designer for several SAR systems and is currently the Deputy Director of the Department of Space Microwave Remote Sensing System, IECAS. His current research interests include airborne and spaceborne SAR system design and their signal processing.

Ruishi Wang, photograph and biography not available at the time of publication.

Li Wang received the bachelor's degree in communication engineering from Wuhan University, Wuhan, China, in 2016 and the master of engineering degree in telecommunication from Australia National University, Canberra, ACT, Australia in 2019, and the Ph.D. degree in computer science from the University of Technology Sydney, Ultimo, NSW, Australia in 2022.

He is currently with the Commonwealth Scientific and Industrial Research Organisation, Canberra, Australia. His research interests include efficient learning, graph neural networks, and wearable health monitoring system design.

Daqing Ge was born in Shaanxi, China. He received the B.S. degree in engineering of surveying and mapping from the China University of Mining and Technology (CUMT), Xuzhou, China, in 2002, the M.S. degree in photogrammetry and remote sensing from the China University of Mining and Technology (Beijing) (CUMTB), Beijing, China, in 2005, and the Ph.D. degree in environmental science and engineering from the China University of Geosciences (Beijing) (CUGB), Beijing, in 2013.

He was the Principal Investigator of several Chinese national projects. He is currently a Senior Engineering (Professorship) with the China Aero Geophysical Survey and Remote Sensing Center for Land and Resources, Beijing. His research interests mainly include radar interferometry technology, geohazards monitoring applications, and the development of SAR satellite application systems.

Xiuqing Liu received the graduation degree in communication and information systems from the Institute of Electronics, Chinese Academy of Sciences, Beijing, China, in 2004.

She is currently an Associate Researcher with the Institute of Aerospace Information Innovation, Chinese Academy of Sciences. Her main research interests include polarimetric/compact polarimetric SAR system technology, polarimetric/compact polarimetric SAR data processing, and information extraction.

Chunle Wang received the M.Sc. degree from Beijing Information Science and Technology University, Beijing, China, in 2008, and the Ph.D. degree from the Graduate University of Chinese Academy of Sciences, Beijing, in 2013, both in communication and information systems.

Currently, she is an Associate Research Assistant in SAR system design and their image processing with the Institute of Electronic, Chinese Academy of Science. Her current research interests include classification and polarimetric target decomposition technique for polarimetric synthetic aperture radar.

Bin Liu received the bachelor's degree in mathematics and applied mathematics from the Shandong University of Science and Technology, Qingdao, China, in 2005 and the master's degree in geodesy and survey engineering from the Shandong University of Science and Technology, Qingdao, in 2009, the Ph.D. degree in disaster mitigation and prevention engineering from the Institute of Engineering Mechanics, China Earthquake Administration, Harbin, China, in 2013.

His thesis was on SAR interferometry application on land subsidence survey. He is currently with the China Aero Geophysical Survey and Remote Sensing Center for Natural Resource, Beijing, China. He is engaged in theoretical and applied research on spaceborne, airborne, and ground-based interferometric synthetic aperture radar (SAR).